Niobium-Doped Titanium Dioxide with High Dopant Contents for Enhanced Lithium-Ion Storage

Wenlei Xu,[a] Patrícia A. Russo,*[a] Thorsten Schultz,[b, c] Norbert Koch,[b, c] and Nicola Pinna*[a]

Titanium dioxide is a promising anode for efficient lithium-ion storage in terms of low cost, good structural stability, and inherent safety. However, its performance in Li-ion storage is hindered by poor electronic conductivity. In this work, a solvothermal approach was applied for the synthesis of Nb-doped TiO_2 nanocrystals with Nb content up to 33 at.%. The enhanced electronic conductivity and favorable electrochemical kinetics led to superior specific capacity, rate capability, and cycling stability compared to pristine TiO_2. For the optimum dopant content of 21 at.%, a specific capacity of 58 $mAh\,g^{-1}$ was reached at 10 $A\,g^{-1}$ compared to just 28 $mAh\,g^{-1}$ for pure TiO_2, in addition to almost 20% higher capacity retention after prolonged cycling. The strategy in the current work can be easily extended to the design of other high-performance electrode materials for energy storage.

1. Introduction

Rechargeable lithium ion batteries (LIBs) have been widely used in our daily life as the main power sources for electric vehicles and portable electronic devices such as laptops, tablets and handheld devices.[1] To meet the future requirements for various types of electric vehicles, numerous types of electrode materials have been investigated to improve the LIBs properties, especially nanostructured materials because of their advantages like larger electrode/electrolyte contact area and shortened Li^+ diffusion distances.[2] Among them, transition metal oxides have been extensively studied as electrode materials for LIBs.[2e,3]

Titanium dioxide (TiO_2) in the anatase structure is environmentally benign, low cost, highly abundant, stable and safe during cycling, making it a promising anode material for LIBs.[4] However, pristine TiO_2 exhibits low electronic conductivity (ca. 10^{-12}–10^{-7} $S\,cm^{-1}$), slow Li^+ diffusion rate (ca. 10^{-15}–10^{-9} $cm^2\,s^{-1}$), and frequent aggregation of TiO_2 nanoparticles, which leads to poor rate capability and cycling stability.[5] Various strategies have been used to overcome the ionic and electronic transport limitations and improve the electrochemical performance of titania anodes, such as fabricating TiO_2 composite structures,[4a,6] and reducing particle size.[7] Nevertheless, these strategies have some limitations, as the benefits of composite structures are limited to the surface only, whereas reducing particles to nanoscale size can lead in some cases to agglomeration and dissolution during cycling, which results in decreased electroactive area and irreversible capacity losses.[8]

Another effective strategy to enhance the electrical conductivity and electrochemical performance of TiO_2 is incorporating aliovalent ions (such as Nb^{5+}) into the TiO_2 structure,[4c,5,8–9] which is attributed to an increase in donor density. Wang *et al.*[9a] reported that the conductivity of Nb-doped mesoporous TiO_2 was more than two orders of magnitude higher than that of undoped TiO_2. These results are in agreement with the findings of Sheppard *et al.*[10] indicating metallic-type conductivity of reduced Nb-doped TiO_2. Fehse *et al.*[5] demonstrated that the improved rate capability of Nb-doped TiO_2 arises mainly from the enhancement of charge transfer in TiO_2. Substitution of Nb^{5+} for Ti^{4+} introduces additional charge carriers, which increase the low bulk conductivity of TiO_2. It has also been shown that an appropriate Nb concentration is necessary to balance ionic and electronic transport.[4c,9e] Various methods have been applied to produce Nb-doped TiO_2, including the sol-gel method,[4c,9a] continuous hydrothermal flow method,[9d] and electrospinning.[5] However, the amount of Nb incorporated is in most cases lower than 10 at.%,[4c,5,11] which is mainly due to the ultrastable structure of TiO_2 that limits the diffusion and mobility of foreign ions.[12] Furthermore, it has been reported that the introduction of high amounts of dopants may damage the TiO_2 crystal structure, negatively affecting its electrochemical performance.[4c,9e] Therefore, it is still a great challenge to obtain niobium titanium mixed oxide with high Nb contents in stable structures.

Non-hydrolytic sol-gel syntheses strategies using organic solvents are highly effective at producing metal oxide nanocrystals with high purity and compositional homogeneity, such as $BaTiO_3$,[13] TiO_2,[14] or Nb_2O_5.[15] Efficient doping and high dopant contents can also be achieved due to the controlled

[a] W. Xu, Dr. P. A. Russo, Prof. N. Pinna
Institut für Chemie and IRIS Adlershof
Humboldt-Universität zu Berlin
Brook-Taylor-Str. 2, 12489 Berlin, Germany
E-mail: patricia.russo@hu-berlin.de
nicola.pinna@hu-berlin.de
[b] Dr. T. Schultz, Prof. N. Koch
Institut für Physik and IRIS Adlershof
Humboldt-Universität zu Berlin
Brook-Taylor-Str. 2, 12489 Berlin, Germany
[c] Dr. T. Schultz, Prof. N. Koch
Helmholtz-Zentrum Berlin für Materialien und Energie GmbH
Albert-Einstein Str. 15, 12489 Berlin, Germany

Supporting information for this article is available on the WWW under https://doi.org/10.1002/celc.202001040

reactivity of metal precursors in organic solvents.[16] The flexibility of these methods with respect to size and composition allows a wide variety of oxide-based nanostructures to be attained.[17]

Herein, we present a simple solvothermal approach to obtain niobium titanium mixed oxides by reaction of niobium ethoxide and titanium isopropoxide with acetophenone. The as-synthesized materials display superior rate performance and cycling stability in comparison to that of pristine TiO_2. This work provides an innovative strategy to synthesize other metal-based materials with tunable compositions.

2. Results and Discussion

Information on the crystalline structure of the synthesized materials was obtained via X-ray diffraction (XRD) and Raman spectroscopy. The XRD patterns in Figure 1a are indexed to the anatase phase of titanium dioxide (tetragonal, ICDD file no. 021-1272). No obvious reflections from niobium oxide crystalline phases are detected in the patterns, indicating that no segregated crystalline niobium oxide phases are formed. The small reflection at around 14° (2θ) matches the (121) reflection of the TiO_2 brookite phase (ICDD file no. 029-1360), suggesting the formation of a small amount of brookite phase during the synthesis, as found by other authors.[5] The intensity of this reflection increases with increasing Nb concentration, which shows that the incorporation of niobium promotes the formation of the brookite phase. A gradual shift of the (101) reflection to lower diffraction angles is observed with increasing Nb concentration, indicating a gradual increase of the interlayer distance and lattice expansion as the amount of Nb dopant incorporated into the structure increases. The larger ionic radius of Nb^{5+} (0.64 Å) compared to that of Ti^{4+} (0.61 Å), explains the increase of the (101) interplanar distance, which, according to Bragg's equation, results in the decrease of the diffraction angle.[18]

The structural properties of the various niobium titanium mixed oxide materials were also studied by Raman spectroscopy (Figure 1b). For the pure TiO_2, six Raman-active modes appear at 151 (E_g), 204 (E_g) 405 (B_{1g}), 522 ($A_{1g}+B_{1g}$), and 645 cm^{-1} (E_g), which correspond to the TiO_2 anatase phase, in agreement with the phase obtained from XRD.[19] No obvious brookite related modes are observed in the Raman spectrum, which could be due to the negligible amount of brookite phase. In the Nb incorporated TiO_2 spectra, the strong Raman band at ca. 151 cm^{-1}, related to O–Ti–O bending, is shifted to higher wavenumbers for all samples.[5,20] A number of factors could be related to the changes of the Raman band positions and intensities, such as pressure, particle size, and dopants.[18b,21] Shifts in Raman are associated with changes in the local structure, such as strains in the structure, defects or distortions. The shift to higher wavenumbers is consistent with lattice expansion occurring upon introduction of Nb into the TiO_2 structure, as Nb^{5+} is larger than Ti^{4+}. However, the magnitude of the shift is smaller for NTO-3 compared to NTO-1 and NTO-2. The smaller shift for NTO-3 can be attributed to the strain created in the structure by the higher concentration of Nb, which has an opposite effect on the wavenumber. The band width at 151 cm^{-1} increased with increasing Nb concentration, which can be attributed to the formation of Nb–O–Ti bonds.[22] At the same time, the band at 645 cm^{-1} got broader and more intense because of the formation of Nb–O bonds.[22]

Transmission electron microscopy (TEM) and high-resolution TEM (HRTEM) were performed to investigate the morphology and microstructure of the samples. As shown in Figure 2 and S1, nearly spherical nanoparticles are produced through this synthesis method. These materials have a similar particle size (around 10 nm in diameter). Nano-sized particles allow fast lithium-ion intercalation and deintercalation due to the short distances for lithium-ion transport within the particles. The HRTEM image in Figure 2a reveals the highly crystalline nature of TiO_2 with an interplanar spacing of 0.353 nm, corresponding to the (101) lattice planes of the tetragonal crystalline structure of anatase. The interplanar spacing is slightly larger for the doped materials (Figure 2c, S1), which is consistent with the substitution of Ti^{4+} cations (ionic radius = 0.61 Å) with larger Nb^{5+} (ionic radius = 0.64 Å) in the structure, in agreement with the XRD results. The expanded interlayer spacing is thought to be beneficial for the insertion/deinsertion process of lithium

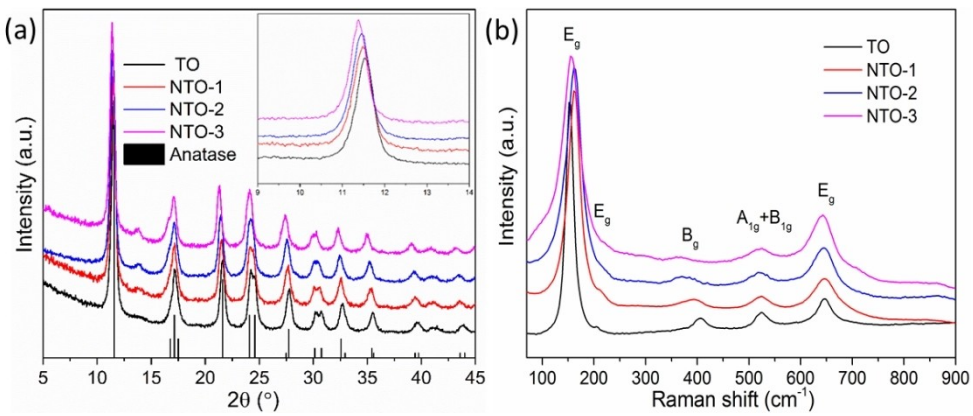

Figure 1. a) X-ray diffractograms (vertical bars indicate the anatase reference: ICDD file no. 021-1272) and b) Raman spectra of the TO (pure TiO_2), NTO-1 (10 mol% Nb), NTO-2 (20 mol% Nb), and NTO-3 (30 mol% Nb) samples. The inset in figure (a) shows the magnified view of the most intense reflection (101).

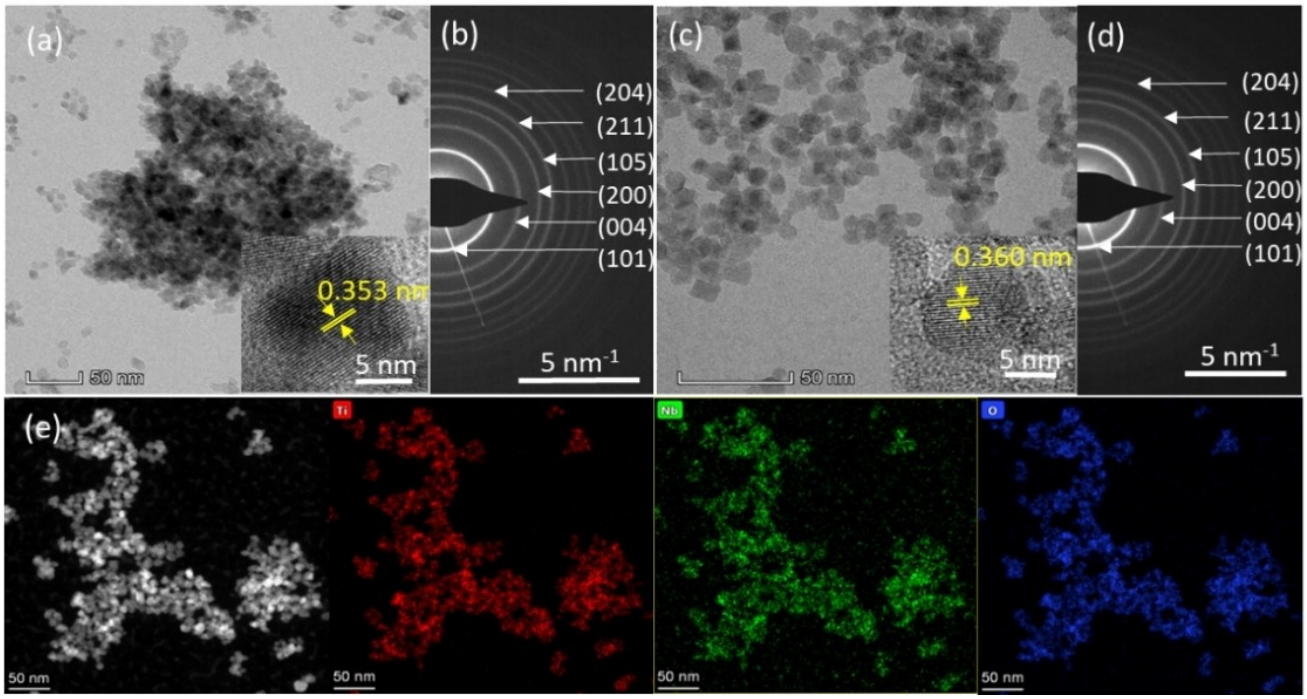

Figure 2. TEM and HRTEM (inset) images of a) TO and c) NTO-2; SAED of b) TO and d) NTO-2; e) STEM-HAADF image and corresponding EDX elemental maps of NTO-2.

ions within the doped TiO_2 lattice.[23] The selected area electron diffraction (SAED) patterns (Figure 2b, 2d, S1b and S1d) confirm that all the samples are crystalline and match the anatase TiO_2 structure. Energy dispersive X-ray spectroscopy (EDX) analysis for NTO-1, NTO-2 and NTO-3 (Figure S2, Table S1) shows that the Nb content is 9, 21 and 33 at.%, respectively, which is close to the nominal ratios. EDX mapping (Figure 2e and S1) shows the homogeneous distribution of the elements (Ti, O and Nb), further suggesting the successful doping of the TiO_2 matrix.

The chemical states of all samples were investigated by X-ray photoelectron spectroscopy (XPS). Figure 3a presents the high-resolution Ti 2p XPS spectra. For the pure TiO_2, the Ti 2p core level binding energies were 458.3 eV (Ti $2p_{3/2}$) and 464 eV (Ti $2p_{1/2}$) with a splitting energy of 5.7 eV, which are consistent with titanium in its Ti^{4+} oxidation state.[24] For Nb modified TiO_2, the binding energies gradually shift to higher values, which indicates a shift of the Femi level position towards the conduction band.[25] Besides, the bands are broadened compared to pure TiO_2, which could be due to structural disorder after Nb introduction. In the case of Nb (Figure 3b), a doublet at binding energies of 206.7 eV (Nb $3d_{5/2}$) and 209.5 eV (Nb $3d_{3/2}$) can be observed in the Nb 3d XPS spectra, suggesting that Nb is present in the 5+ oxidation state.[26] Based on these data, it can be concluded that the charge compensation of Nb^{5+} in substitution of Ti^{4+} can be achieved by the formation of cation vacancies.[25] Figure 3c shows the O 1s XPS spectra. The main signal at 529.6 eV, which can be assigned to Ti–O bonds, shifts to higher binding energies after Nb incorporation in the same way as the Ti 2p signals, because of the Fermi level shift mentioned above. The other two signals at 532.1 eV and 533.6 eV are ascribed to surface OH groups and adsorbed H_2O, respectively.[27] Furthermore, from the valence band region of all the samples (Figure 3d), a clear shift of the valence band onset to higher binding energies is seen after Nb incorporation. This is because Nb^{5+} is a donor-type dopant for TiO_2, introducing a donor state in the band gap. The additional Nb 4d electron pushes the Fermi level closer to the conduction band, thus improving the electric conductivity.[25]

Cyclic voltammetry (CV) was carried out to evaluate the lithium storage behavior of the samples. Figure 4a and S3a show the typical CV curves of NTO-2 and TO for the first three cycles at a scan rate of 0.1 mV s^{-1}. Both samples exhibit some capacity loss after the initial scan, which is mainly due to side reactions with the electrolyte and irreversible Li^+ insertion. Redox peaks at 1.72/1.97 V (NTO-2) and 1.67/2.04 V (TO) represent lithiation and delithiation processes in anatase, which is consistent with the discharge/charge potential plateaus of the galvanostatic curves (Figure 5a and S4a). Moreover, a small peak pair at ~1.48 and ~1.8 V can be seen for both NTO-2 and TO, which might be attributed to a second phase transition from $Li_{0.55}TiO_2$ to Li_1TiO_2.[6d,28] NTO-2 exhibits a smaller potential deviation between anodic and cathodic peaks (ΔE: 0.25 V) compared to that of TO (ΔE: 0.37 V). This implies faster Li^+ insertion-deinsertion kinetics for the Nb containing TiO_2 sample, resulting from the higher electron and ionic conductivity as well as larger interplanar spacing offered by Nb incorporation, as it will be discussed below.[19,29] For the Nb-doped samples, a small anodic peak appears at ~2.7 V, whose intensity increases with increasing scan rate. As no clear corresponding cathodic

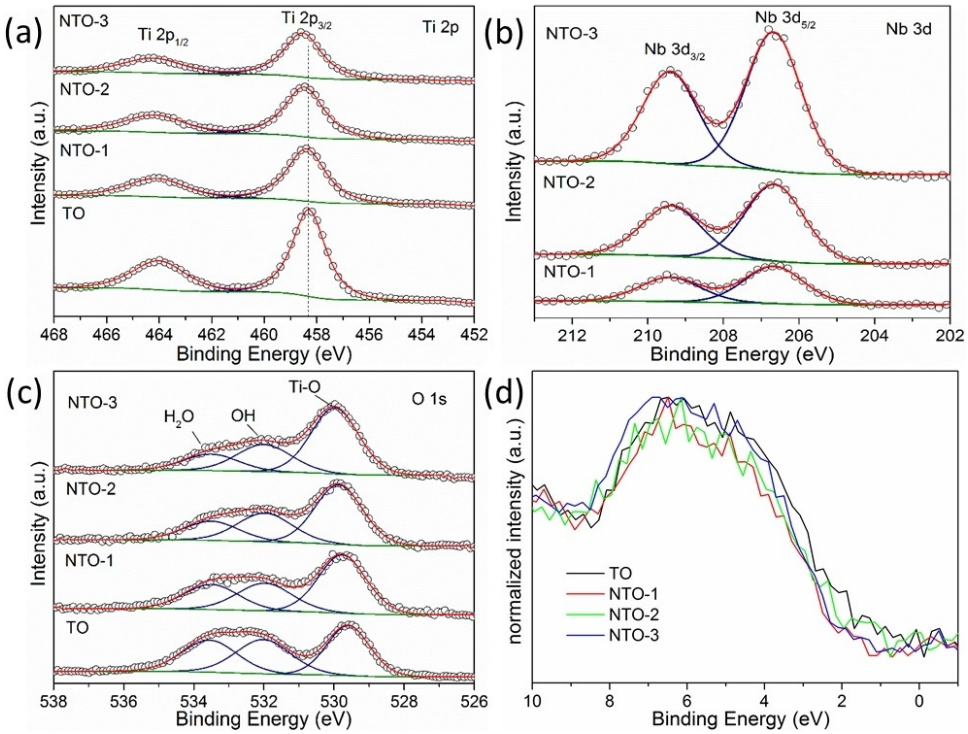

Figure 3. High resolution X-ray photoelectron spectra of a) Ti 2p, b) Nb 3d, c) O 1s and d) valence band XPS spectra for all the samples.

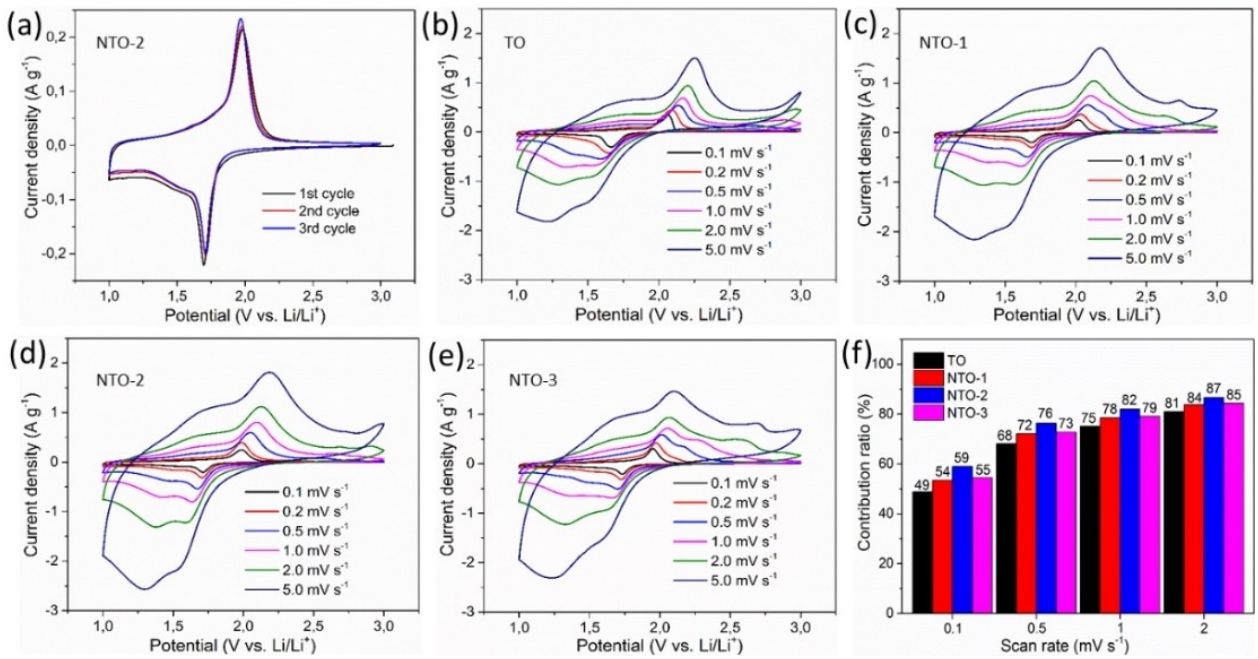

Figure 4. a) CV curves of NTO-2 during the first three cycles at a scan rate of 0.1 mV s^{-1}. CV curves at various scan rates from 0.1 to 5 mV s^{-1} for b) TO, c) NTO-1, d) NTO-2, and e) NTO-3. f) The contribution of capacitive to the total charge storage of the samples at different scan rates.

peaks can be seen, the process seems to be irreversible or partly reversible, and likely caused by a side reaction.

Galvanostatic charge/discharge (GCD) measurements were done to evaluate the electrochemical performance of the samples. As shown in Figure 5a and S4, the initial discharge and charge capacities for TO, NTO-1, NTO-2, and NTO-3 are 216 and 175, 208 and 163, 212 and 172, 208 and 167 mAh g^{-1}, corresponding to initial Coulombic efficiencies of 81%, 78%, 82%, and 80%, respectively. The initial capacity loss during the first cycle is attributed to the irreversible reduction of electro-

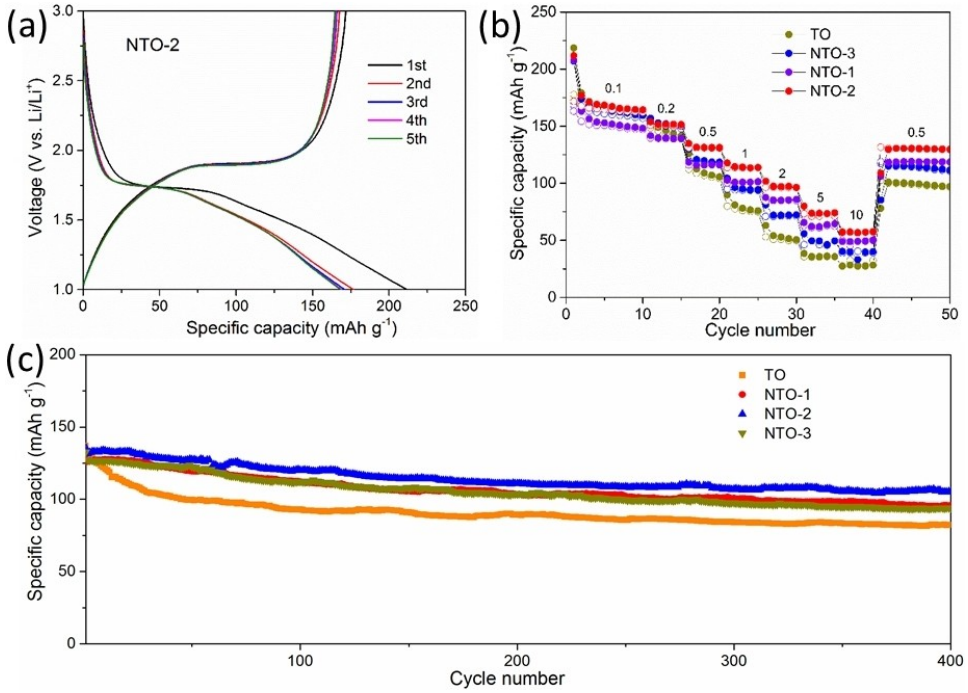

Figure 5. a) First 5 galvanostatic discharge-charge voltage profiles of NTO-2 at 0.1 A g^{-1}. b) Specific capacities at current densities between 0.1 and 10 A g^{-1} for TO, NTO-1, NTO-2 and NTO-3. c) Cycling stability of TO, NTO-1, NTO-2 and NTO-3 at 0.5 A g^{-1}.

lyte and the formation of a solid electrolyte interphase (SEI) layer on the surface of TiO_2, as well as the trapping of Li^+ in irreversible sites.[8,15a,34]

The rate performance of TiO_2 and Nb-doped TiO_2 electrodes was evaluated at different specific current densities from 0.1 to 10 A g^{-1}. As shown in Figure 5b and S5, the difference between the specific capacities of TiO_2 and that of niobium doped titanium dioxides increases significantly with increasing current densities, demonstrating the improved rate capability of Nb doped TiO_2 at high current densities as an anode material for Li^+ storage, which is attributed to the improved electrical conductivity offered by cation vacancies and its stable structure. NTO-2 displays the highest reversible capacities at different current densities among the four samples. Reversible charge-discharge specific capacities of 167, 152, 132, 114, 98, and 74 mAh g^{-1} are achieved for NTO-2 at 0.1, 0.2, 0.5, 1, 2, and 5 A g^{-1}, respectively (Figure S5c). At the highest current density of 10 A g^{-1}, the specific capacity for NTO-2 (58 mAh g^{-1}) is higher than that of TO (28 mAh g^{-1}), NTO-1 (50 mAh g^{-1}), NTO-3 (40 mAh g^{-1}). Moreover, when the current density returns to 0.1 A g^{-1}, the capacity of NTO-2 recovers to 131 A g^{-1}, demonstrating the reversibility and structural stability. Compared to the lithium storage performance of other Nb modified TiO_2 anatases (Table S2), NTO-2 exhibits enhanced high rate capability and extraordinary stability, due to the effective synergistic effect of Ti^{4+} vacancies and its stable structure.[34a,35] It is worth noting that NTO-2 achieved higher rate performance than NTO-3. This is probably because excessive Nb^{5+} introduction into the TiO_2 lattice can cause the anatase structure to partially collapse, leading to poor reversibility.[9c,e]

The electrochemical stability of all samples was determined by cycling at 0.5 A g^{-1} (Figure 5c). Figure 5c shows that the specific capacity for NTO-2 after 400 cycles is 105 mAh g^{-1}, with a capacity retention of 80%. On the other hand, TO, NTO-1, and NTO-3 have a capacity retention of 63%, 76%, and 74%, respectively. The cycling stability measurements show the high reversibility and structural stability of the NTO-2 upon Li^+ insertion-deinsertion compared to the pure TiO_2 and also the other doped samples.

The electrochemical impedance spectra (EIS) of pure and Nb modified TiO_2 samples were measured to gain insight into the influence of Nb incorporation on the electrical conductivity (Figure 6). The proposed equivalent circuit is also included in the figure. The small intercept of the semicircle at the horizontal

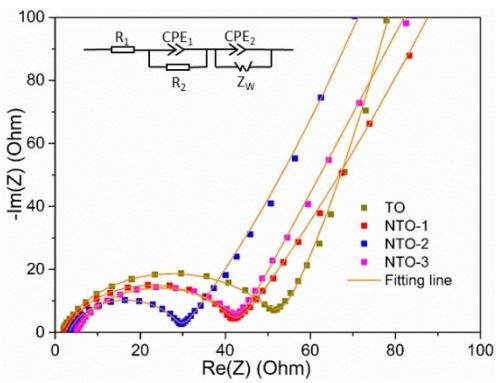

Figure 6. Impedance spectra of TO, NTO-1, NTO-2 and NTO-3, including the equivalent circuit.

axis represents the bulk resistance (R_1) of electrolyte, separator, and electrode, the semicircle corresponding to R_2 is the charge transfer resistance at the electrode/electrolyte interface, CPE_1 and CPE_2 are constant phase elements, and an inclined line denoted as Z_w (Warburg resistance) is ascribed to the semi-infinite diffusion of the lithium ions in the electrode. The fitted resistant values are listed in Table S3. The fitted results indicated that NTO-2 exhibits the lowest R_2 (25.82 Ω). The lower resistance results in faster electron and ion transport during the charge-discharge processes, as previously observed for other Nb-doped TiO_2.[5,9d] Undoped TiO_2, as expected, has the lowest conductivity, while the conductivity increases with the increase of the Nb content up to 21% and subsequently decreases for the Nb content of 33%, showing that excessive Nb^{5+} doping in TiO_2 can be detrimental for the conductivity of the material and electrochemical performance. The minimum resistance achieved with the NTO-2 material contributes to its enhanced Li-ion storage performance.

Figure 4b–e show the representative CV curves for TO, NTO-1, NTO-2 and NTO-3 at various sweep rates, which are used to evaluate capacitive contribution to the total charge storage. All the CV curves show gradually broadened peaks, and the voltammograms become more rectangular, indicating extrinsic capacitive charge storage properties.[9d] The area under the CV curve represents the total charge storage, which arises from both capacitive and diffusion-controlled insertion processes.[30] The measured current (i, A) obeys a power law relationship with the sweep rate (v, $V s^{-1}$) [Eq. (1)]:[31]

$$i = av^b \quad (1)$$

Where a and b are adjustable values. In particular, a b-value of 0.5 indicates the current response is diffusion-controlled, while a b-value of 1 indicates that the current is surface-controlled. As shown in figure S3b, the b values for peak 1 and 4 are 0.59 and 0.49, indicating that the diffusion-controlled process is dominant. Whereas the b values for peak 2 and 3 are 0.87 and 0.82, suggesting a larger capacitive-type contribution. Additionally, the different charge storage mechanisms can be distinguished quantitatively according to the formula [Eq. (2)]:[32]

$$i = k_1 v + k_2 v^{1/2} \quad (2)$$

In equation (2), $k_1 v$ (b = 1) and $k_2 v^{1/2}$ (b = 0.5) represent surface capacitive effects and diffusion-controlled contribution, respectively. k_1 and k_2 are constants for a certain potential. A plot of $i\,(V)/v^{1/2}$ vs. $v^{1/2}$ allows for the calculation of k_1 and k_2 and thus the capacitive and diffusion contributions for each potential. Figure 4f shows that the capacitive contribution increases with increasing sweep rate. Notably, Nb-doped TiO_2 show higher capacitive contribution than that of pure TiO_2, and NTO-2 exhibits the highest value at different scan rates. The maximum value of NTO-2, up to 87% when the sweep rate increased to 2 $mV s^{-1}$, determines a favorable Li-ion storage behavior under high current densities. The improved capacitive behavior is mainly a benefit from Nb incorporation. Because Nb^{5+} is an electron donor type dopant, the introduction of Nb increases the electrical conductivity of the samples, which increases the migration rate of the Li ions at the electrode/electrolyte interface, rendering greater capacitive charge storage. The incorporation of Nb also generates lattice distortions and other defects that provide abundant active sites for Li^+ reaction at the electrode surface, inducing more capacitive charge storage capability. These defect sites allow for fast Li^+ storage without causing a large volume expansion, thus resulting in high rate capability and cycling stability.[19,33] As a consequence, robust and fast lithium storage for NTO-2 was achieved at high rates.

3. Conclusions

Niobium modified titanium dioxide materials were synthesized via a facile, generally applicable nonaqueous route. Nb was homogeneously incorporated within the anatase TiO_2 nanocrystals at the titanium sites, with concentrations of 9, 21 and 33 at.%, resulting in changes in the electronic structure and the creation of additional sites for Li^+ reaction. When studied as anode materials for Li-ion storage, the sample with 21 at.% exhibits improved rate capability and cycling stability, delivering a specific capacity at 10 $A g^{-1}$ of 58 $mAh g^{-1}$ compared with 28, 50 and 40 $mAh g^{-1}$ for pure TiO_2, 9% doped and 33% doped TiO_2, respectively. The enhanced electrochemical performance can be ascribed to its increased electronic conductivity and structural stability.

Experimental Section

Material Synthesis

Titanium dioxide nanocrystals doped with niobium were synthesized through a simple solvothermal method. For preparing the 20 mol% Nb-containing TiO_2 nanoparticles, 0.2 mmol of niobium(V) ethoxide (99.9%, abcr) and 0.8 mmol of titanium(IV) isopropoxide (97%, Sigma-Aldrich) were added to 10 mL of acetophenone (99%, Sigma-Aldrich) in a 30 mL glass vial, and stirred at room temperature for 10 min in a glovebox under Ar. Then the solution was transferred into a stainless steel autoclave with a Teflon liner, and carefully sealed. The autoclave was heated in an oven at 220 °C for 48 h. The products were collected by centrifugation and thoroughly washed with acetone and ethanol, and dried at 70 °C under air. Samples with other Nb contents (0, 10, and 30 mol%) were prepared by following the same procedure. The samples are denoted TO, NTO-1, NTO-2, and NTO-3 for Nb contents of 0, 10, 20, and 30 mol%, respectively.

Characterization

XRD patterns were recorded with a STOE MP diffractometer in transmission configuration using Mo Kα radiation (λ = 0.70930 Å). Transmission electron microscopy (TEM) and high resolution TEM (HRTEM) images were obtained on a Philips CM 200 and FEI Talos 200S microscope operated at 200 kV. Raman spectra were obtained on a DXR Raman spectrometer (Thermo Scientific) with a 532 nm laser for illumination. The scattered light from the sample was dispersed by a 1200 gr/mm grating and collected by an Olympus microscope with a 100x objective. The Spectra were recorded from accumulation of 5 scans × 60 s acquisition time. X-ray photoelectron

spectroscopy measurements were performed using a JEOL JPS-9030 setup with a base pressure of 3×10^{-9} mbar, employing the K_{α}-radiation of a non-monochromated Mg X-ray source ($h\nu=$ 1253.6 eV) for excitation and a hemispherical analyzer to detect the kinetic energy of the emitted electrons. The powders were evenly distributed on carbon tape and measured without further treatment. The C 1s C–C core level was set to 284.8 eV binding energy as a reference since the samples were charging.

Electrochemical Measurements

The working electrodes were made by homogeneously mixing active materials (TO, NTO-1, NTO-2, and NTO-3), conductive carbon black (Super P, Timcal) and polyvinylidene fluoride (PVDF, Alfa Aesar) as a binder in a weight ratio of 7:2:1 with N-methyl-2-pyrrolidone (NMP, anhydrous 99.5%, Sigma-Aldrich) as solvent. The resulting slurry was uniformly cast on copper foil (Goodfellow, UK) with a doctor blade apparatus and dried in a vacuum oven at 60 °C for 1 hour. After a cold-laminating step, electrodes with a diameter of 18 mm were punched out and dried overnight at 120 °C under vacuum using a Büchi glass oven. The active material mass loadings at the anodes was in the range of 1.0 to 1.2 mg cm^{-2}.

Electrochemical experiments were performed using CR2032-type coin cells, which were assembled in an Ar-filled glovebox. Lithium metal foil was used as both counter and reference electrodes. 1 M LiPF6 (ABCR, 99.9% battery grade) solution in a mixture of ethylene carbonate (EC, 99.9%, ABCR), diethyl carbonate (DEC, 99.9%, ABCR) and dimethyl carbonate (DMC, 99.9%, ABCR) with 1:1:1 volume ratio was used as the electrolyte. A glass microfiber filter (Whatman) was used as a separator.

Galvanostatic charge-discharge cycling was carried out at room temperature using a CT2001 A battery testing system (Landt Instruments) in the potential window of 1.0 to 3.0 V versus Li/Li$^+$ at specific currents in the range of 0.1 to 10 A g^{-1}. Cyclic voltammograms (CVs) were measured on a Bio-Logic VMP3 multichannel potentiostat/ galvanostat with a built-in electrochemical impedance spectroscopy (EIS) analyzer, in the potential range of 1.0 to 3.0 V vs. Li/Li$^+$ with a scan rate in the range of 0.1 to 5 mV s^{-1}. EIS was performed at open-circuit potential (OCP), in the frequency range of 100 kHz to 10 mHz with an amplitude of 10 mV.

Acknowledgements

W. X. acknowledges the fellowship from the China Scholarship Council (CSC). Open access funding enabled and organized by Projekt DEAL.

Conflict of Interest

The authors declare no conflict of interest.

Keywords: Nb-doped TiO_2 · high Nb content · enhanced electronic conductivity · anode materials · lithium-ion storage

[1] a) C. Choi, D. S. Ashby, D. M. Butts, R. H. DeBlock, Q. Wei, J. Lau, B. Dunn, *Nat. Rev. Mater.* **2020**, *5*, 5; b) Q. Wei, F. Xiong, S. Tan, L. Huang, E. H. Lan, B. Dunn, L. Mai, *Adv. Mater.* **2017**, *29*, 1602300.
[2] a) K. Liu, Y. Liu, D. Lin, A. Pei, Y. Cui, *Sci. Adv.* **2018**, *4*, eaas9820; b) Y.-K. Sun, Z. Chen, H.-J. Noh, D.-J. Lee, H.-G. Jung, Y. Ren, S. Wang, C. S. Yoon, S.-T. Myung, K. Amine, *Nat. Mater.* **2012**, *11*, 942; c) R. Schmuch, R. Wagner, G. Hörpel, T. Placke, M. Winter, *Nat. Energy* **2018**, *3*, 267; d) P. G. Bruce, B. Scrosati, J.-M. Tarascon, *Angew. Chem. Int. Ed.* **2008**, *47*, 2930; e) J. Jiang, Y. Li, J. Liu, X. Huang, C. Yuan, X. W. Lou, *Adv. Mater.* **2012**, *24*, 5166.
[3] M. Wagemaker, F. M. Mulder, *Acc. Chem. Res.* **2013**, *46*, 1206.
[4] a) B. Y. Guan, L. Yu, J. Li, X. W. Lou, *Sci. Adv.* **2016**, *2*, e1501554; b) S.-T. Myung, M. Kikuchi, C. S. Yoon, H. Yashiro, S.-J. Kim, Y.-K. Sun, B. Scrosati, *Energy Environ. Sci.* **2013**, *6*, 2609; c) J. Yue, C. Suchomski, P. Voepel, R. Ellinghaus, M. Rohnke, T. Leichtweiss, M. T. Elm, B. M. Smarsly, *J. Mater. Chem. A* **2017**, *5*, 1978; d) B. Xu, S. Qi, M. Jin, X. Cai, L. Lai, Z. Sun, X. Han, Z. Lin, H. Shao, P. Peng, Z. Xiang, J. E. ten Elshof, R. Tan, C. Liu, Z. Zhang, X. Duan, J. Ma, *Chin. Chem. Lett.* **2019**, *30*, 2053.
[5] M. Fehse, S. Cavaliere, P. E. Lippens, I. Savych, A. Iadecola, L. Monconduit, D. J. Jones, J. Rozière, F. Fischer, C. Tessier, L. Stievano, *J. Phys. Chem. C* **2013**, *117*, 13827.
[6] a) G. Zhu, L. Ma, H. Lin, P. Zhao, L. Wang, Y. Hu, R. Chen, T. Chen, Y. Wang, Z. Tie, Z. Jin, *Nano Res.* **2019**, DOI: 10.1007/s12274-019-2427–3; b) Y. F. Yuan, F. Chen, S. M. Yin, L. N. Wang, M. Zhu, J. L. Yang, Y. C. Wu, S. Y. Guo, *J. Power Sources* **2019**, *420*, 38; c) S. Luo, T. Yuan, L. Soule, J. Ruan, Y. Zhao, D. Sun, J. Yang, M. Liu, S. Zheng, *Adv. Funct. Mater.* **2020**, *30*, 1908309; d) L. Sun, W. Liu, R. Wu, Y. Cui, Y. Zhang, Y. Du, S. Liu, S. Liu, H. Wang, *Nanoscale* **2020**, *12*, 746; e) S. Huang, L. Zhang, X. Lu, L. Liu, L. Liu, X. Sun, Y. Yin, S. Oswald, Z. Zou, F. Ding, O. G. Schmidt, *ACS Nano* **2017**, *11*, 821.
[7] a) M. Wagemaker, W. J. H. Borghols, F. M. Mulder, *J. Am. Chem. Soc.* **2007**, *129*, 4323; b) Y. Ren, Z. Liu, F. Pourpoint, A. R. Armstrong, C. P. Grey, P. G. Bruce, *Angew. Chem. Int. Ed.* **2012**, *51*, 2164.
[8] T. V. Thi, A. K. Rai, J. Gim, S. Kim, J. Kim, *J. Alloys Compd.* **2014**, *598*, 16.
[9] a) Y. Wang, B. M. Smarsly, I. Djerdj, *Chem. Mater.* **2010**, *22*, 6624; b) Z. Ali, S. N. Cha, J. I. Sohn, I. Shakir, C. Yan, J. M. Kim, D. J. Kang, *J. Mater. Chem.* **2012**, *22*, 17625; c) H. He, D. Sun, Q. Zhang, F. Fu, Y. Tang, J. Guo, M. Shao, H. Wang, *ACS Appl. Mater. Interfaces* **2017**, *9*, 6093; d) D. Bauer, A. J. Roberts, S. G. Patnaik, D. J. L. Brett, P. R. Shearing, E. Kendrick, N. Matsumi, J. A. Darr, *J. Electrochem. Soc.* **2018**, *165*, A1662; e) D. Yan, C. Yu, D. Li, X. Zhang, J. Li, T. Lu, L. Pan, *J. Mater. Chem. A* **2016**, *4*, 11077.
[10] L. R. Sheppard, T. Bak, J. Nowotny, *J. Phys. Chem. B* **2006**, *110*, 22447.
[11] A. J. Gardecka, M. Lübke, C. F. Armer, D. Ning, M. V. Reddy, A. S. Williams, A. Lowe, Z. Liu, I. P. Parkin, J. A. Darr, *Solid State Sci.* **2018**, *83*, 115.
[12] Y. Pan, Z. Luo, Y.-C. Chang, K.-C. Lau, C. Y. Ng, *J. Phys. Chem. A* **2017**, *121*, 669.
[13] M. Niederberger, G. Garnweitner, N. Pinna, M. Antonietti, *J. Am. Chem. Soc.* **2004**, *126*, 9120.
[14] G. Garnweitner, M. Antonietti, M. Niederberger, *Chem. Commun.* **2005**, DOI: 10.1039/B414510 K397.
[15] a) X. Han, P. A. Russo, N. Goubard-Bretesché, S. Patanè, S. Santangelo, R. Zhang, N. Pinna, *Adv. Energy Mater.* **2019**, *9*, 1902813; b) K. Skrodczky, M. M. Antunes, X. Han, S. Santangelo, G. Scholz, A. A. Valente, N. Pinna, P. A. Russo, *Commun. Chem.* **2019**, *2*, 129.
[16] a) S. Wahl, S. M. El-Refaei, A. G. Buzanich, P. Amsalem, K.-S. Lee, N. Koch, M.-L. Doublet, N. Pinna, *Adv. Energy Mater.* **2019**, *9*, 1900328; b) X. Han, S. Wahl, P. A. Russo, N. Pinna, *Nanomaterials* **2018**, *8*, 249.
[17] a) N. Pinna, M. Niederberger, *Angew. Chem. Int. Ed.* **2008**, *47*, 5292; b) Z. Wei, B. Ding, H. Dou, J. Gascon, X.-J. Kong, Y. Xiong, B. Cai, R. Zhang, Y. Zhou, M. Long, J. Miao, Y. Dou, D. Yuan, J. Ma, *Chin. Chem. Lett.* **2019**, *30*, 2110.
[18] a) X. Lü, X. Mou, J. Wu, D. Zhang, L. Zhang, F. Huang, F. Xu, S. Huang, *Adv. Funct. Mater.* **2010**, *20*, 509; b) X. Lü, W. Yang, Z. Quan, T. Lin, L. Bai, L. Wang, F. Huang, Y. Zhao, *J. Am. Chem. Soc.* **2014**, *136*, 419; c) A. K. Chandiran, F. Sauvage, M. Casas-Cabanas, P. Comte, S. M. Zakeeruddin, M. Graetzel, *J. Phys. Chem. C* **2010**, *114*, 15849.
[19] Q. Gan, H. He, Y. Zhu, Z. Wang, N. Qin, S. Gu, Z. Li, W. Luo, Z. Lu, *ACS Nano* **2019**, *13*, 9247.
[20] A. J. Gardecka, G. K. L. Goh, G. Sankar, I. P. Parkin, *J. Mater. Chem. A* **2015**, *3*, 17755.
[21] H. C. Choi, Y. M. Jung, S. B. Kim, *Vib. Spectrosc.* **2005**, *37*, 33.
[22] a) L. De Trizio, R. Buonsanti, A. M. Schimpf, A. Llordes, D. R. Gamelin, R. Simonutti, D. J. Milliron, *Chem. Mater.* **2013**, *25*, 3383; b) H. Su, Y.-T. Huang, Y.-H. Chang, P. Zhai, N. Y. Hau, P. C. H. Cheung, W.-T. Yeh, T.-C. Wei, S.-P. Feng, *Electrochim. Acta* **2015**, *182*, 230.
[23] a) A. Ghicov, M. Yamamoto, P. Schmuki, *Angew. Chem. Int. Ed.* **2008**, *47*, 7934; b) H.-S. Kim, J. B. Cook, H. Lin, Jesse S. Ko, Sarah H. Tolbert, V. Ozolins, B. Dunn, *Nat. Mater.* **2016**, *16*, 454.

[24] R. P. Netterfield, P. J. Martin, C. G. Pacey, W. G. Sainty, D. R. McKenzie, G. Auchterlonie, *J. Appl. Phys.* **1989**, *66*, 1805.
[25] A. M. Ruiz, G. Dezanneau, J. Arbiol, A. Cornet, J. R. Morante, *Chem. Mater.* **2004**, *16*, 862.
[26] a) M. K. Bahl, *J. Phys. Chem. Solids* **1975**, *36*, 485; b) N. Singh, M. N. Deo, M. Nand, S. N. Jha, S. B. Roy, *J. Appl. Phys.* **2016**, *120*, 114902.
[27] L. T. Anh, A. K. Rai, T. V. Thi, J. Gim, S. Kim, E.-C. Shin, J.-S. Lee, J. Kim, *J. Power Sources* **2013**, *243*, 891.
[28] a) C. Li, M. Zhao, C. N. Sun, B. Jin, C. C. Yang, Q. Jiang, *J. Power Sources* **2018**, *397*, 162; b) J. Brumbarov, J. P. Vivek, S. Leonardi, C. Valero-Vidal, E. Portenkirchner, J. Kunze-Liebhäuser, *J. Mater. Chem. A* **2015**, *3*, 16469.
[29] a) Y. Xing, S. Wang, B. Fang, G. Song, D. P. Wilkinson, S. Zhang, *J. Power Sources* **2018**, *385*, 10; b) M. Lübke, J. Shin, P. Marchand, D. Brett, P. Shearing, Z. Liu, J. A. Darr, *J. Mater. Chem. A* **2015**, *3*, 22908.
[30] J. Wang, J. Polleux, J. Lim, B. Dunn, *J. Phys. Chem. C* **2007**, *111*, 14925.
[31] a) V. Augustyn, J. Come, M. A. Lowe, J. W. Kim, P.-L. Taberna, S. H. Tolbert, H. D. Abruña, P. Simon, B. Dunn, *Nat. Mater.* **2013**, *12*, 518; b) H. Lindström, S. Södergren, A. Solbrand, H. Rensmo, J. Hjelm, A. Hagfeldt, S.-E. Lindquist, *J. Phys. Chem. B* **1997**, *101*, 7717.
[32] a) S. Ardizzone, G. Fregonara, S. Trasatti, *Electrochim. Acta* **1990**, *35*, 263; b) V. Augustyn, E. R. White, J. Ko, G. Grüner, B. C. Regan, B. Dunn, *Mater. Horiz.* **2014**, *1*, 219.
[33] a) N. Wu, X. Qiao, J. Shen, G. Liu, T. Sun, H. Wu, H. Hou, X. Liu, Y. Zhang, X. Ji, *Electrochim. Acta* **2019**, *299*, 540; b) B. Hao, Y. Yan, X. Wang, G. Chen, *ACS Appl. Mater. Interfaces* **2013**, *5*, 6285.
[34] a) Z. Hao, Q. Chen, W. Dai, Y. Ren, Y. Zhou, J. Yang, S. Xie, Y. Shen, J. Wu, W. Chen, G. Q. Xu, *Adv. Energy Mater.* **2020**, *10*, 1903107; b) J.-Y. Shin, D. Samuelis, J. Maier, *Adv. Funct. Mater.* **2011**, *21*, 3464; c) H. Wang, J. He, J. Liu, S. Qi, M. Wu, J. Wen, Y. Chen, Y. Feng, J. Ma, *Adv. Funct. Mater.* DOI: 10.1002/adfm.202002578.
[35] F. Lu, Q. Chen, S. Geng, M. Allix, H. Wu, Q. Huang, X. Kuang, *J. Mater. Chem. A.* **2018**, *6*, 24232.

Manuscript received: August 7, 2020
Revised manuscript received: September 3, 2020
Accepted manuscript online: September 21, 2020